

An Aggregation-Volume-Bias Monte Carlo Investigation on the Condensation of a Lennard-Jones Vapor below the Triple Point and Crystal Nucleation in Cluster Systems: An In-Depth Evaluation of the Classical Nucleation Theory

Bin Chen,* Hyunmi Kim, Samuel J. Keasler, and Ricky B. Nellas

Department of Chemistry, Louisiana State University, Baton Rouge, Louisiana 70803-1804

Received: October 3, 2007; In Final Form: January 7, 2008

The aggregation-volume-bias Monte Carlo based simulation technique, which has led to our recent success in vapor–liquid nucleation research, was extended to the study of crystal nucleation processes. In contrast to conventional bulk-phase techniques, this method deals with crystal nucleation events in cluster systems. This approach was applied to the crystal nucleation of Lennard-Jonesium under a wide range of undercooling conditions from 35% to 13% below the triple point. It was found that crystal nucleation in these model clusters proceeds initially via a vapor–liquid like aggregation followed by the formation of crystals inside the aggregates. The separation of these two stages of nucleation is distinct except at deeper undercooling conditions where the crystal nucleation barrier was found to diminish. The simulation results obtained for these two nucleation steps are separately compared to the classical nucleation theory (CNT). For the vapor–liquid nucleation step, the CNT was shown to provide a reasonable description of the critical cluster size but overestimate the barrier heights, consistent with previous simulation studies. On the contrary, for the crystal nucleation step, nearly perfect agreement with the barrier heights was found between the simulations and the CNT. For the critical cluster size, the comparison is more difficult as the simulation data were found to be sensitive to the definition of the solid cluster, but a stringent criterion and lower undercooling conditions generally lead to results closer with the CNT. Additional simulations at undercooling conditions of 40% or above indicate a nearly barrierless transition from the liquid to crystalline-like structure for sufficiently large clusters, which leads to further departure of the barrier height predicted by the CNT from the simulation data for the aggregation step. This is consistent with the latest experimental results on argon that show an unusually large underestimation of the nucleation rate by the CNT toward deep undercooling conditions.

1. Introduction

Nucleation refers to a broad range of phenomena where embryos of a new phase are formed in a metastable supersaturated mother phase. Being an activated event, nucleation is a critical first step in phase transitions. In particular, for cases when multiple phases (or structures) with similar thermodynamic stabilities are accessible, nucleation may become the crucial kinetic factor in determining the preference for the final structure/phase. An important example is crystallization where molecules can be brought together to form various ordered arrays (or polymorphs). Each of the polymorphs formed has unique physical and chemical properties. Therefore, polymorphism control has important implications in areas from the tailor-design of nanoparticles to the manufacture of pharmaceutical compounds.^{1,2} However, our ability to exercise this type of control remains limited because of our lack of knowledge about the molecular level details of the crystal nucleation process.

Experimentally, the molecular characterization of the crystal nucleation event is hampered by the activated nature of this process and the difficulty in probing and quantifying both the thermodynamic and the structural properties of the clusters formed at the early stage. In particular, critical nuclei that appear at the top of the free energy barrier are not amenable to direct experimental observation as they are small and transient and their occurrence probabilities are extremely low. Nevertheless,

it is the structure and dynamics of these small clusters that determine the kinetics of the nucleation event.³ On the other hand, the atomistic details about these early clusters cannot be derived directly from the century-old classical nucleation theory (CNT).^{4–10} Although this theory allows the prediction of the size of the critical nucleus and the nucleation barrier height, this information is obtained under the assumption that clusters have a spherical shape and behave like an infinite bulk phase with regard to density and surface tension, despite the fact that they are finite objects. As shown for vapor–liquid nucleation, the neglect of the molecular details about clusters and their distinct behavior from bulk phases is actually the major shortcoming responsible for the serious discrepancies observed between the results predicted by the CNT and those measured by the experiments (e.g., see refs^{11–14}). For crystal nucleation (starting from a monomeric phase), an additional complication to CNT is that this event may pass through other phases before turning into the ordered structure adopted by the bulk. For example, the clusters formed in the initial stage of the nucleation process are likely to be in a disordered phase because small clusters are well-known to have significantly lower melting points than bulk crystals.

In recent years, great strides have been made in the field of molecular simulation that have enabled the use of this atomistic approach in the study of the nucleation phenomena. Molecular simulation has several intrinsic advantages for this endeavor. Apart from providing rich microscopic information, it can be

* Corresponding author. E-mail: binchen@lsu.edu.

used to test the assumptions made by the CNT and also compare directly to other theoretical approaches (such as density functional theory) for a consistent model. In addition, complex and realistic force fields can be employed by this approach, and the results can be compared directly to the experiment. For example, recent technical advances in the vapor–liquid nucleation area have allowed a side-by-side comparison to the experimental nucleation rate data for various systems (see ref 15 for the latest work). While a similar transformation is happening in the crystal nucleation area, most of the research carried out there is directed toward crystallization in an undercooled bulk liquid phase, instead of the conventionally encountered crystallization from a solution or directly from a vapor with the monomer as the starting point. In addition, the degree of undercooling is often too high to access experimentally. In this work, we took advantage of the simulation advances made recently in both vapor–liquid and crystal nucleation research and developed a combined approach that allows a simulation investigation of the crystal nucleation events involved in continuously growing clusters at even low undercooling conditions.

In the next section, the technical details of this combined approach are presented followed by a brief description of the other simulation details involved in this study. The simulation results are presented and discussed in section 3, and section 4 provides concluding remarks.

2. Simulation Methods and Details

A. AVUS-HR Approach The AVUS-HR^{16,17} technique that led to our recent success in simulating a series of rare vapor–liquid nucleation events is a major component of this crystal nucleation approach. As an activated event, nucleation can be characterized by a nucleation free energy (NFE) profile expressed as a function of order parameters, for example, cluster size in vapor–liquid nucleation. Constructing this NFE landscape becomes the major task for simulation, but this is extremely demanding computationally for conventional techniques. The AVUS-HR approach was developed for this purpose through a combination of a few advanced simulation techniques, including aggregation-volume-bias Monte Carlo (AVBMC),^{18,19} configurational-bias Monte Carlo (CBMC),^{20–22} umbrella sampling (US),²³ and histogram reweighting (HR),^{24,25} to overcome the several types of difficulties present in the sampling of the nucleation event. One particular challenge to simulation posed by the nucleation system is the coexistence of a spectrum of microphase regions, for example, monomer and clusters (which differ to a great extent in both energetic and entropic factors). While frequent cluster growth and destruction are required for a smooth interpretation of the cluster distribution or the corresponding NFE, conventional methods such as the Metropolis²⁶ Monte Carlo scheme and molecular dynamics are very inefficient for these moves, hampered either by the low (entropic) probability to attempt cluster growth or by the low acceptance rate (or large energetic penalty) for cluster destruction. AVBMC^{18,19} balances these two factors for both cluster growth and destruction by employing direct particle transfer between the cluster and the mother phase. In this case, cluster growth is no longer governed by the entropic factor (i.e., large spatial separations or density differences between the monomer and the cluster). On the other hand, to satisfy the detailed balance condition, this entropic factor enters the acceptance rule for the reverse move (i.e., cluster destruction) which compensates for the energetic penalty, yielding an enhanced acceptance rate. The incorporation of the configurational-bias Monte Carlo (CBMC)^{20–22}

scheme further improves the acceptance rates for the AVBMC swaps and most importantly allows the extension of this method to molecules with articulated structures.

Although more frequent cluster growth/destruction events can be sampled via a combination of AVBMC and CBMC, the statistical probability of visiting a cluster (of a given size and structure) is still governed by its NFE value. Because of the large barrier heights involved in typical nucleation events, the probabilities of observing clusters near the barrier remain extremely low, sometimes $O(10^{-30})$ (relative to that of monomer). Without bias, the convergence of the cluster probability distribution (or NFE) from the simulation would be impossible (as it requires at least $O(10^{30})$ steps, an unattainable task even with the current terascale computer platforms). In this regard, US²³ is introduced to help flatten the barriers on the NFE landscape through an iterative addition of biasing potentials so that clusters of all sizes and structures of interest can be sampled within a reasonable simulation length, and the bias introduced can be removed later in the analysis of the cluster distribution. To further minimize the computational expense, this combined technique allows us to single out one cluster from the entire system for both AVBMC swap moves and the umbrella biasing. By turning this global problem into a local one, the size of the system required for the simulation is greatly reduced, whereas the distribution information obtained from this single cluster can be directly used for constructing the cluster probability distribution of the whole system. This reduced system size also makes it natural to integrate HR^{24,25} with this technique as large energy fluctuations are expected for small systems. HR is useful in that predictions can be made for a range of thermodynamic conditions using the existing simulation data collected at a very limited set of conditions.

B. Extension of the AVUS-HR Approach to the Crystal Nucleation Study in Cluster Systems The extension of the AVUS-HR technique to crystal nucleation events in clusters of growing size is straightforward except that additional order parameters are required in order to define the crystallinity of the system. While the size of the cluster remains a major order parameter (which is defined through the Stillinger²⁷ cluster criterion with a distance cut off of 1.5σ , following our previous work for Lennard-Jonesium¹¹), the Steinhardt²⁸ order parameter Q_6 was used to quantify the degree of crystallinity in the cluster. Q_6 has been frequently used by previous crystal nucleation simulations in bulk systems because of its several desirable features.^{3,29–31} For example, it can be made independent of the orientation of the system in space. While this order parameter is indicative of the overall degree of crystallinity in the system (e.g., it vanishes for a bulk liquid phase but takes a large value for many crystal lattices of interest), it is not so sensitive to the type of crystal structure adopted by the system.³ Thus, the use of Q_6 would not bias the simulation toward formation of a particular crystal structure. Following previous crystal nucleation studies on bulk-phase systems, the value of Q_6 is computed for the clusters as follows,

$$Q_6 = \left(\frac{4\pi}{13} \sum_{m=-6}^6 \left| \bar{Q}_{6m} \right|^2 \right)^{1/2} \quad (1)$$

with

$$\bar{Q}_{6m} = \frac{1}{N_b} \sum_{n=1}^{N_b} Y_{6m}(\hat{\mathbf{r}}_{ij}) \quad (2)$$

where N_b denotes the number of bonded pairs (a pair is considered bonded here as long as the distance between them is less than 1.5σ), $Y_{6m}(\hat{\mathbf{r}}_{ij})$ is the m th component of the sixth order spherical harmonics whose value also depends on the orientation of the unit vector $\hat{\mathbf{r}}_{ij}$ defined between a given bonded pair of molecules i and j .

C. Construction of the Multi-Dimensional NFE Surface

The addition of Q_6 creates another dimension for the free energy surface that needs to be computed in the crystal nucleation simulation. Similar to the multicomponent vapor–liquid nucleation,^{15,17} a multidimensional biasing potential is employed with values chosen as the negative of the NFEs, that is, $-\Delta G(n, Q_6)$, to allow for clusters of all sizes and crystallinity involved in the crystal nucleation to be sampled evenly by the simulation. Since Q_6 is a continuous variable, in collecting the cluster distribution information, a bin width of 0.01 is used for constructing these histograms (and correspondingly for the interpretation of NFEs and umbrella biasing potentials as well).

Following previous work,¹¹ the NFEs were constructed through an iterative procedure. Initially, all simulations were started by iterating the NFEs along the cluster size coordinate. Considering the wide range of clusters (from monomer up to clusters containing a few thousand particles) to be sampled for most cases, multiple simulations were employed with each covering a small “window” of cluster sizes (e.g., a cluster size range of 10 was used here). These windows need not be fully overlapped. In fact, in the simulations described here, they were separated from each other as much as possible with a roughly even spacing of 100 molecules between two adjacent windows toward high cluster size range. Since the required number of clusters to be sampled in each window is rather small, the convergence of the NFE data can be achieved within a very short CPU time (from a few seconds for small clusters to a couple of hours for larger clusters). After full convergence, the gradients of these NFE data with respect to the cluster size were computed. A smooth fit to a polynomial function was performed for these discretized gradient data. By integrating the resulting polynomial function, the NFE data were obtained over the entire range of the cluster size. A polynomial fit for interpreting nucleation data has been used previously.³²

Using the NFE data obtained above (originally expressed as function of only the cluster size), we created a two-dimensional biasing potential by expanding this profile along the Q_6 order parameter (i.e., with initially no bias on this crystallinity coordinate or a bias interpreted from data obtained at a neighboring simulation condition). The simulations were then allowed to sample clusters of the entire size and order range using this two-dimensional biasing potential. Multiple (16 or 32) independent runs were used to collect the cluster distribution information $P(n, Q_6)$. The length of these runs for each iteration varies from a few hours for the low-temperature cases to a few days for the high-temperature cases. After each iteration, the NFEs were interpreted, that is, $\Delta G(n, Q_6) = -k_B T \ln P(n, Q_6)$. For the low-temperature cases (where the barrier heights along Q_6 are low), usually a couple of iterations were required before we started to see formation of clusters with a high degree of crystallinity. Since finding the lowest barrier that needs to be crossed over along the Q_6 coordinate is our major concern here, from the point when the crystal free energy minimum began to develop on the nucleation landscape, the largest bias (called the threshold bias) that can be applied along the Q_6 coordinate was fixed to a nearby integer value based on the maximum bias used in previous iterations. This allows later iterations to be focused on the most important part of the NFE surface. In

addition, the initial configurations were carefully selected to be on the low crystallinity side to further narrow down the simulation sampling toward the portion of the NFEs along the Q_6 coordinate that are crucial for the determination of the crystal nucleation barrier.

D. Other Simulation Details All simulations described here were performed for the Lennard-Jonesium (LJ) system. For computational efficiency, these simulations were carried out using the grand-canonical version of the nucleation algorithm¹¹ where a single cluster is completely isolated from the rest of the system and the chemical potential of the gas-phase (or the number density of the ideal gas phase, n_v) is directly specified as part of the simulation conditions. While the interactions between the cluster and the surrounding environment (a vapor-phase here) are neglected in these calculations, they are expected to play a minor role in the crystal nucleation process as it occurs inside the cluster. This approximation also makes the configurational integral (or the Helmholtz free energy) of a cluster at any size n become independent of the chemical potential of the gas-phase.^{11,33} Thus, the NFE values (relative to that of the monomer) obtained at one gas-phase chemical potential μ can be conveniently used to calculate those at any other condition μ' as follows,

$$\Delta G_{\mu'}(n) = \Delta G_{\mu}(n) - (n - 1) \times (\mu - \mu') \quad (3)$$

For this system, the total energy was computed by summing up all pair interactions. The type of Monte Carlo move in each step was randomly selected between AVBMC swaps and translation with equal probabilities. For the former move, the CBMC technique with multiple insertions of the first bead was used to enhance the acceptance rate.^{11,34,35} While for the translational move, the maximum displacement was fixed at 0.2σ . Four temperatures were selected: 0.45, 0.5, 0.55, and 0.6 (in reduced units), which correspond to an undercooling condition of 35%, 27%, 20%, and 13% with respect to the bulk-phase triple point of $0.689 (T_t)$,³⁶ respectively. The maximum cluster size was chosen large enough so that the crystal clusters start to appear as a stable minimum on the free energy landscape. While an increase of the temperature lowers the relative stabilities of crystalline clusters versus disordered ones, an increase of the cluster size has the opposite effect. Therefore, in order to obtain a stable crystal cluster at higher temperatures, the maximum cluster size has to be set at larger values. For example, for the four temperatures considered here (in increasing order), the maximum cluster size is set at 400, 800, 1600, and 3600 respectively.

3. Simulation Results and Discussions

A. NFE as Function of Cluster Size. Given the large number of clusters sampled by these simulations, the distribution of NFEs is expected to be broad. This was directly reflected by Figure 1, where the NFE data, projected as a function of cluster size only, spanned over a rather wide range, for example, from -450 to $300 k_B T$ for the highest temperature case. For all temperatures, these curves were plotted at a gas-phase activity where the nucleation barrier height reaches $300 k_B T$. While this barrier is too high to cross over in practice, as will be shown later the sizes of the critical clusters obtained with respect to this aggregation coordinate (which are located at the barrier positions shown in Figure 1) are still too small to form a stable crystal inside. Even smaller critical clusters are expected for more realistic barrier heights (around $50 k_B T$) that can be accessed by experiment.

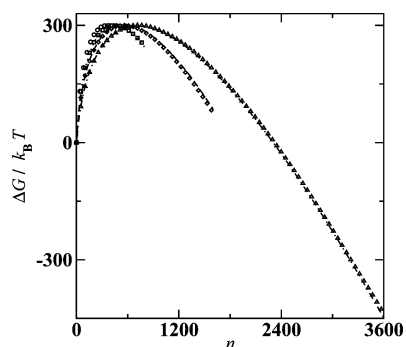


Figure 1. NFEs as a function of the cluster size at $T = 0.45$ and $n_v = 1.037 \times 10^{-5}$ (black circles), $T = 0.5$ and $n_v = 4.731 \times 10^{-5}$ (squares), $T = 0.55$ and $n_v = 1.596 \times 10^{-4}$ (diamonds), and $T = 0.6$ and $n_v = 4.324 \times 10^{-4}$ (triangles). The results interpolated from polynomial fits to the discretized data obtained from the use of multiple non-overlapping windows are also shown as dotted, dashed, and dotted-dashed lines for $T = 0.5$, 0.55 , and 0.6 , respectively.

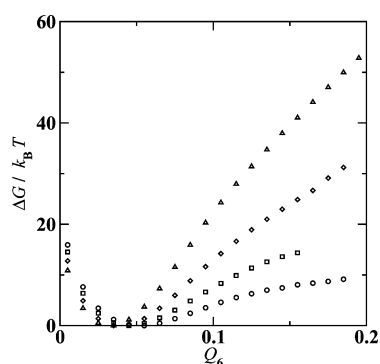


Figure 2. NFEs as a function of the Steinhardt Q_6 order parameter for the critical clusters encountered in the aggregation step (determined based on the NFE profiles shown in Figure 1). Symbols are as those in Figure 1.

Therefore, for this LJ type of system, the crystal nucleation process can be literally decoupled from the aggregation step as it occurs for much larger clusters that are positioned on the other side of these NFE profiles (i.e., after the critical barrier for the aggregation step is surpassed). Since this aggregation process (which governs the rate of droplet formation) still behaves pretty much as a vapor–liquid type of nucleation event even for conditions far below T_i , when applying CNT to predict the rate (or the barrier height) for the droplet formation, the input macroscopic properties (such as density and surface tension) should be derived from the (undercooled) liquid phase instead of the stable crystalline phase. A detailed comparison to CNT is made later in section 3.C.

It should be noted that the results interpolated from polynomial fits on data yielded by simulations using multiple small windows (as described in Section 2C) were also included in Figure 1. While the polynomial interpolation scheme has saved more than an order magnitude of CPU time compared with conventional iterations carried out over the entire cluster size range, the results produced by this approximate method were found to be nearly identical to the final converged data.

B. NFE as Function of the Steinhardt Order Parameter Q_6 . For the critical clusters obtained from the NFE profiles shown in Figure 1 (i.e., determined along the aggregation coordinate only), the data were further analyzed and plotted against the Q_6 parameter (see Figure 2). It is evident from this figure that for all cases only one free energy minimum (FEM) could be identified at a low Q_6 position, which corresponds to a liquid-like structure and will be referred to as the LFEM (the

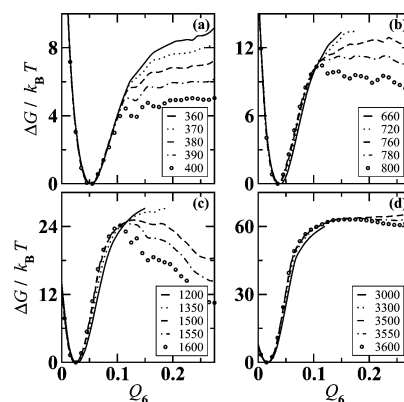


Figure 3. NFEs as a function of the Steinhardt Q_6 order parameter for growing clusters with sizes specified in the figure. The results calculated at $T = 0.45$, 0.5 , 0.55 , 0.6 are separately shown in panels a, b, c, and d, respectively.

NFE data shown here were actually plotted on a relative scale with respect to the LFEM). Note that cluster systems, even when their structures are fully disordered, would still take a small, finite Q_6 value instead of zero as expected for bulk liquid phases. Only at the lowest temperatures (e.g., $T = 0.45$) did the NFE data appear to approach a plateau toward large Q_6 (where crystalline clusters were located), while these results were already above the threshold bias imposed on this coordinate required for the formation of stable crystalline clusters. For example, at $T = 0.45$ a threshold bias of $5 k_B T$ was found sufficient for the crystal nucleation event to occur during the simulation, which has a typical length of $O(10^6)$ Monte Carlo cycles. The threshold bias increased to $10 k_B T$ at $T = 0.5$, $24 k_B T$ at $T = 0.55$, and up to $63 k_B T$ at $T = 0.6$.

Given that crystal nucleation events occur after the critical barrier for the aggregation step has been surpassed, we turned our focus to larger clusters. It is clear from Figure 3 that with the growth of the clusters, a stable crystalline free energy minimum (CFEM), eventually appeared on the NFE landscape. Note that the NFE data shown in this figure were also shifted (similar to Figure 2) by setting the LFEM as the zero point for all clusters of different sizes, so that the barrier encountered in the crystal nucleation could be examined separately from the cluster growth. This way of plotting also allows a direct view of how the crystal nucleation part of the profile evolves with the growing cluster size. For example, we can see a clear resemblance between these profiles obtained for a wide range of cluster sizes at the low Q_6 region (up to about 0.1), just before these profiles started to approach a maximum. In contrast, after that point, the NFE curves deviated further and further away from each other with the increase of Q_6 . These deviations arise partly from an initial absence of the CFEM for small clusters versus a steadily growing CFEM, which became deeper and wider with the increase of the cluster size. Despite these large deviations, the crystal nucleation barrier height separating this CFEM from the LFEM was fairly similar for clusters of different sizes, especially for the high-temperature cases. For example, at $T = 0.55$ a barrier height of $25.1 k_B T$ was determined for clusters with 1500 particles versus $24.2 k_B T$ for those containing 1600 particles, while at $T = 0.6$ the crystal nucleation barrier height stayed nearly constant around $63.3 k_B T$ for clusters with a size range from 3500 to 3600. On the contrary, at the low temperatures, the barrier heights determined from these curves showed slightly larger scatterings, for example, from $12.3 k_B T$ to $10.4 k_B T$ at $T = 0.5$ for clusters containing from 760 to 800 particles. In addition, with the temperature decreased down to

TABLE 1: Number Density of the Liquid Phase at Coexistence (ρ_1), Vapor–Liquid Surface Tension (γ), and Chemical Potential Difference ($\Delta\mu$, in Units of $k_B T$) between the Saturated and Supersaturated Vapor Phase Used in Obtaining Those NFE Profiles Shown in Figure 1; Subscripts Give the Statistical Accuracies of the Last Decimal(s)

T	ρ_1	γ^a	γ^b	$\Delta\mu^a$	$\Delta\mu^b$
0.45	0.9411 _c		1.739		−1.821
0.5	0.9224 ₁		1.627	−1.458 ₁₅	−1.443
0.55	0.9032 ₁	1.509 ₅	1.512	−1.153 ₁₂	−1.148
0.6	0.8835 ₁	1.397 ₈	1.395	−0.919 ₉	−0.917

^a Results obtained from the simulations using the techniques and procedures described previously.^{16,38–44} ^b Results interpolated from Figure 4. ^c Results determined from polynomial fits on the T -dependency of the liquid-phase density.

0.45 (which is 35% below T_l), locating the barrier itself became rather difficult as the NFE data appeared to reach a plateau toward high Q_6 . However, a precise determination of the barrier for such low-temperature cases may not be so critical. As mentioned before, a threshold bias of 5 $k_B T$ was already high enough to let crystal nucleation take place within very short simulation length scales. The crystal nucleation barrier at $T = 0.45$ was thus expected to be very low (probably around the magnitude of 5 $k_B T$). In fact, without any bias an additional isobaric–isothermal ensemble simulation at this temperature for a bulk-phase system starting from a liquid-like state (containing 864 particles in a box surrounded by its periodic images) yielded a crystalline configuration after only 10,000 Monte Carlo cycles. This spontaneous crystallization process has been also reported previously for LJ bulk liquids at such deep undercooling conditions.³⁰ In addition, recent work on a gold cluster of 456 particles has suggested that freezing becomes barrierless at low temperatures.³⁷

C. Comparison with the Classical Nucleation Theory, the Experiment, and Previous Theoretical Studies. In CNT,^{4–7} the free energy of formation for a cluster with a radius of r in a homogeneous bulk phase is broken into two contributions, one from the surface free energy and the other from the chemical potential difference ($\Delta\mu$) between the two phases involved in a particular phase transition,

$$\Delta G = 4\pi r^2 \gamma + \frac{4}{3} \pi r^3 \rho \Delta\mu \quad (4)$$

To make this calculation simpler, in CNT, the cluster takes a compact and spherical shape, which allows for a convenient quantification of r . Furthermore, the cluster is assumed to behave like a bulk phase (of an infinite size) so that the rest of the terms involved in the above formula, including surface tension γ and density ρ , can be borrowed directly from the corresponding macroscopic properties that are accessible by experiments. By maximizing ΔG , the critical nucleation barrier height can be obtained in terms of these macroscopic properties,

$$\Delta G^* = \frac{16\pi\gamma^3}{3\rho^2\Delta\mu^2} \quad (5)$$

The radius at which ΔG reaches this maximum is given by

$$r^* = \frac{2\gamma}{\rho|\Delta\mu|} \quad (6)$$

with a corresponding cluster size of

$$n^* = \frac{32\pi\gamma^3}{3\rho^2|\Delta\mu|^3} \quad (7)$$

r^* and n^* are the most important microscopic data about the critical clusters (and are often the only molecular details) that can be provided within the framework of CNT.

The above set of equations is applicable to both vapor–liquid and crystal nucleation. For the latter type, CNT is restricted to the nucleation of crystal nuclei in a homogeneous bulk phase (e.g., in an infinite liquid system). The crystal nucleation process described here is clearly more complicated as it initially proceeds along a vapor–liquid type of nucleation, followed by the formation of crystal nuclei inside the liquid-like clusters. Fortunately, on the basis of the above analysis of the NFE data obtained for the LJ cluster system, it becomes possible to separate these two stages of nucleation. Therefore, in the following discussion, comparison to the CNT was made individually for either nucleation step.

Comparison with CNT on the Vapor–Liquid Nucleation Barrier Height and Critical Cluster Size. For the initial vapor–liquid nucleation step, in order to compare to CNT, additional simulations using bulk-phase systems and the procedure outlined in previous work were carried out to determine the vapor–liquid surface tension^{38–41} and the coexistence properties^{16,42–44} for this LJ model with the final results listed in Table 1. It should be noted that at the lowest temperatures these properties were difficult to obtain directly from such bulk-phase simulations due to the instability of the liquid and the associated spontaneous crystallization. For those low- T conditions (i.e., $T = 0.45$ and 0.5), both γ and $\Delta\mu$ were actually extracted from the NFE data. It has been shown^{14,45} that for sufficiently large clusters, the change in NFE with respect to the cluster size n follows the CNT description as prescribed below,

$$\delta\Delta G(n) = \Delta G(n) - \Delta G(n-1) = (A_n - A_{n-1})\gamma + \Delta\mu \quad (8)$$

where A_n is the surface area, which is proportional to $n^{2/3}$ in CNT. Thus, by plotting $\delta\Delta G(n)$ against the change of the surface area (or $n^{2/3} - (n-1)^{2/3}$), a linear plot is expected which intercepts with the y axis at $\Delta\mu$ with a slope governed by γ (see Figure 4). To validate this interpolation scheme, for the two high- T cases, both γ and $\Delta\mu$ determined from the linear plots shown in Figure 4 were listed in Table 1 to compare with those calculated directly from the bulk-phase simulations. It is evident that the two sets of data are in excellent agreement with each other.

By substituting the surface tension and liquid density data into eqs 5 and 7, predictions can be made by the CNT on the nucleation barrier height and critical cluster size at various gas-phase conditions. Given those CNT equations, the predicted results were plotted as a function of either $(\Delta\mu)^{-3}$ for n^* in Figure 5 or $(\Delta\mu)^{-2}$ for ΔG^* in Figure 6 so that they simply fall on a straight line with the slope governed by the surface tension and the bulk liquid density at coexistence. Also included in these figures were the simulation results determined by applying eq 3 to the calculated NFE profiles shown in Figure 1, which follow the straight-line behavior with a slope comparable to the CNT curves especially at the low supersaturation conditions. In fact for the critical cluster sizes, the two curves (either from the simulation or from the CNT) nearly coincide with each other (see Figure 5) except down to critical clusters consisting of 20–30 particles, which mirrors exactly the $\delta\Delta G$ data shown in Figure 4. This correlation between these two figures is expected

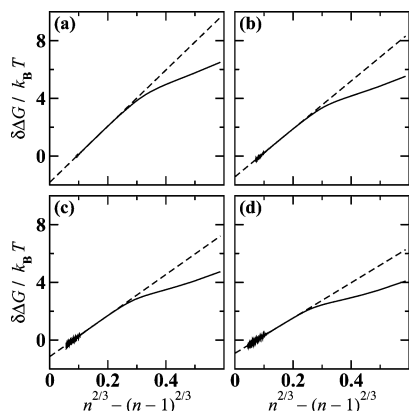


Figure 4. $\delta\Delta G(n)$ results analyzed from the NFE profiles shown in Figure 1 (solid) versus those predicted by the CNT (dashed) plotted as a function of $n^{2/3} - (n-1)^{2/3}$. Results obtained at the four temperatures are shown in separate panels as those in Figure 3.

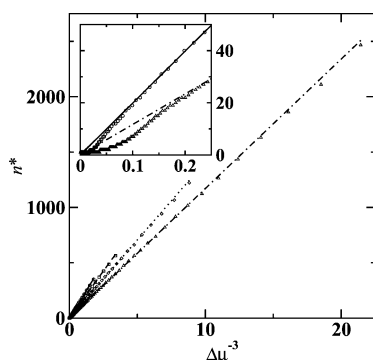


Figure 5. Critical cluster size (in the aggregation step) as a function of $(\Delta\mu)^{-3}$ at $T = 0.45$ (solid line and circles), 0.5 (dashed line and squares), 0.55 (dotted line and diamonds), and 0.6 (dashed-dotted line and triangles). Symbols and lines represent the results obtained from the simulation and the CNT, respectively. The inset is used to magnify the deviations between these two sets of data toward high supersaturation conditions, where the critical clusters are small.

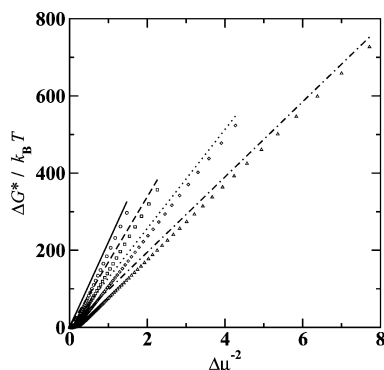


Figure 6. Nucleation barrier height (in the aggregation step) as a function of $(\Delta\mu)^{-2}$. Symbols are as those in Figure 5.

as the critical cluster size is determined by the point where the $\delta\Delta G$ curve crosses zero and the $\delta\Delta G$ curves obtained at different supersaturation conditions are parallel to each other with intercepts dictated by $\Delta\mu$, according to eq 8. On the other hand, given that both the CNT and the simulation predict similar critical cluster sizes and that the two $\delta\Delta G$ curves (yielded either from the simulation or from the CNT) would remain the same on a relative scale at different $\Delta\mu$ conditions, the deviations in $\delta\Delta G$ for the initially formed droplets would contribute to a supersaturation independent offset of ΔG^* (and ΔG in general

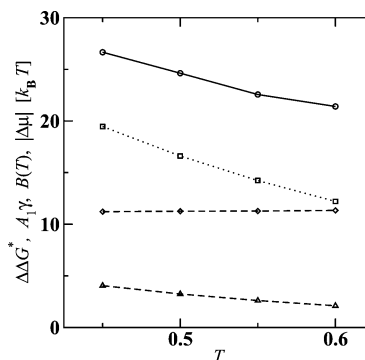


Figure 7. Nucleation barrier height difference observed between the CNT and the simulation ($\Delta\Delta G^*$; represented by circles) as a function of the temperature. These $\Delta\Delta G^*$ were obtained at conditions when the simulation predicted barrier height is $40 k_B T$. The several contributions to this difference, i.e., $A_1\gamma$, $B(T)$, and $|\Delta\mu|$, were shown as squares, diamonds, and triangles, respectively.

for clusters of the same size as long as they are large enough). This offset (called $B(T)$ in ref 14), combined with the difference in the ΔG value of the monomer (i.e., zero in the simulation versus $A_1\gamma - |\Delta\mu|$ in the CNT), accounts for the total deviation in the ΔG^* value shown in Figure 6. Also in agreement with ref 14, $B(T)$ was found to be fairly insensitive to the temperature compared with the rest of the terms, but its range from 11.2 to $11.3 k_B T$ (see Figure 7) is slightly lower than $13.6 k_B T$ reported there for the LJ system. As the contribution of $\Delta\mu$ diminishes toward low supersaturation conditions, the overall offset of ΔG^* is expected to show only the temperature-dependency arising from the $A_1\gamma$ term (i.e., be relatively independent of the supersaturation; see Figure 6).

Comparison with Previous Theoretical Studies and the Latest Experiment on Homogeneous Nucleation Rate of Argon Vapor.

The nucleation results discussed above are consistent with previous simulations for this LJ system,^{11,14,32} which were mostly carried out at temperatures above T_l . Such a constant ΔG^* displacement (from the CNT results) toward low supersaturation was also predicted by density functional theory (DFT) calculations and was put into a simple form of $4\pi k_s$ by McGraw and Laaksonen,⁴⁶ which they explained as a result of the interfacial curvature free energy with k_s denoting the rigidity coefficient. Furthermore, both their studies and ours show a similar temperature dependence for these ΔG^* offsets that apparently agrees also with the temperature-dependent discrepancies observed between CNT and the latest experiment by Fladerer and Strey⁴⁷ on argon vapor. However, direct comparison to the experiment is difficult as the nucleation properties (NFE barrier heights and nucleation rate) were found to be extremely sensitive to the details of the molecular interactions incorporated in the force fields. This is already reflected by the CNT equations where ΔG^* is proportional to γ^3 and inversely proportional to $(\Delta\mu)^2$, which means that even one percent error on either term would cause a few percent deviation in ΔG^* (or a few $k_B T$ in absolute magnitude), and most current force fields are far outside the range of this accuracy. For example, assuming that the argon can be modeled by a LJ potential with an ϵ of 116 K and a σ of 3.39 Å (a parameter set used by the TraPPE force field⁴⁸), the surface tension data calculated here are about 10% higher than the experimental values^{47,49} (see Figure 8). Also, the equilibrium vapor pressure, which is crucial for the determination of $\Delta\mu$, is off by more than 10% from experiment.^{47,50,51} Only the experimental liquid density^{47,52} is reproduced well by this LJ model for argon with an average error of less than 1%. Thus, the comparison made here is on the relative errors of the

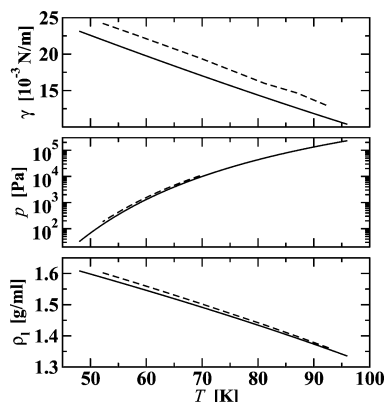


Figure 8. Calculated (dashed) versus experimental (solid) vapor–liquid phase equilibrium properties for argon. γ , p , and ρ_l refer to the surface tension, saturated vapor pressure, and coexistence liquid density, respectively.

CNT compared to either the experiment or the simulation for a consistent system (or model) in predicting the onset conditions for a constant nucleation rate around 10^7 droplets/cm³/s as used by Fladerer and Strey.⁴⁷ From the ΔG^* results obtained above, the nucleation rates were calculated using the following equation,

$$J = J_0 \exp(-\beta \Delta G^*) = \frac{\rho_{\text{vap}}^2}{\rho_{\text{liq}} S} \left(\frac{2\gamma}{\pi m} \right)^{1/2} \exp(-\beta \Delta G^*) \quad (9)$$

where J_0 is the traditional classical prefactor corrected by a factor of $1/S$ (this supersaturation factor is required by CNT for thermodynamic consistency,^{53,54} which can be viewed as a correction to the $\Delta\mu$ term included by the theory for describing the work of formation of the monomer), ρ_{vap} and ρ_{liq} are the densities of the supersaturated vapor and of the liquid phase at coexistence respectively, and m is the molecular mass. Since the nucleation rate is primarily governed by its exponential dependence on ΔG^* , in computing the prefactor, ρ_{vap} is approximately obtained by multiplying the saturated vapor-phase density by the supersaturation while γ and ρ_{liq} were taken directly from Table 1. Shown in Figure 9 were the relative deviations between CNT and experiment (or simulation), described in terms of the ratio of either onset supersaturation or onset pressure. It is clear that the two sets of results are in reasonable agreement with each other at a temperature between 55 and 60 K. This good agreement is expected to extend above this temperature based on the trend of the experimental data. However, below 55 K, the experimental ($p^{\text{CNT}}/p^{\text{EXP}}$) ratios show a sharp increase that leads to a clear departure from their simulation counterpart.

In the work by Merikanto et al.,¹⁴ a roughly constant offset of 2000 Pa to the on-set pressure was reported for their simulation results, which, on a relative scale, would also be translated into larger percentage deviations from the experimental data toward lower temperatures. At these low- T conditions, the experimental on-set pressure is actually on (or even below) this order of magnitude.⁴⁷ Thus, the discrepancies observed for the argon system by the experiments cannot be fully recovered by the errors in the CNT discovered by these simulations for an LJ model. The fact that the sharp increase in the $p^{\text{CNT}}/p^{\text{EXP}}$ ratio happens right on the location where crystalline clusters begin to spontaneously form led us to suggest that the involvement of crystalline clusters may be one possible source of the discrepancies. Although from the above discussions, we seem to completely rule out the interference from the

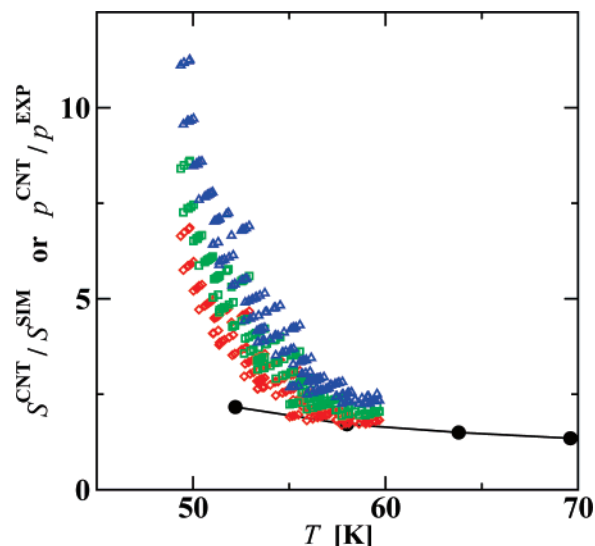


Figure 9. Comparison of onset supersaturation ratio between the CNT and the simulation (circles) to the onset pressure ratio between the CNT and the experiment⁴⁷ (green squares) at an onset nucleation rate of 10^7 droplets/cm³/s. Two additional $p^{\text{CNT}}/p^{\text{EXP}}$ ratios were obtained at a CNT predicted rate of 10^5 and 10^9 droplets/cm³/s, and they were shown as red diamonds and blue triangles, respectively.

crystalline clusters in the aggregation step, this result was solely based on the LJ model. In fact, in addition to its deficiency in describing the liquid-phase properties for the argon system (as mentioned above), the LJ model is also inadequate for the crystalline phase properties. For example, it under-predicts the triple point for argon, that is, 79.9 K (based on a T_l of 0.689 ϵ^{36} for LJ) versus the experimental value of 83.8 K.⁵⁵ The lower prediction on the triple point implies that the stability of the crystalline-like phases (clusters) is substantially underestimated by this model, which may partly cause the non-involvement of crystalline clusters in the aggregation step found for this LJ model. In order to examine how the presence of the crystalline clusters would affect the aggregation NFE profiles, additional simulations were carried out at lower temperatures (one at 0.35 and the other at 0.4) where crystalline clusters are relatively more stable. The results were analyzed in a similar way to those obtained at $T = 0.45$ except that the surface tension data used in the CNT predictions were extracted from a linear fit to the $\delta\Delta G$ curves obtained at an intermediate cluster size range (e.g., 20 to 88 for $T = 0.35$) as they show large deviations from linear behavior even toward clusters of larger sizes. These deviations were due to the formation of crystalline clusters whose free energies are lower than those of liquid-like clusters. Since in CNT only free energies of liquid-like clusters were considered, these deviations also lead to an overall bigger offset between CNT and the simulation on the predicted ΔG^* toward lower supersaturations where crystalline clusters were involved in the aggregation step (and thus would contribute to the barrier height, see Figure 10). It should be noted that the $\delta\Delta G$ curves show a peculiar dip near a cluster size of 140 at $T = 0.35$, around which the cluster undergoes a disorder-to-order transition. As shown in Figure 10b, at this condition smaller clusters consisting of 130 particles are mostly disordered with Q_6 dominantly taking a low liquid-like value (about 0.06), whereas larger clusters of 150 particles are significantly more ordered with the Q_6 value more than doubled. On the other hand, for clusters of intermediate sizes, the crystalline order parameter exhibits a bimodal distribution, showing that both liquid- and crystalline-like clusters coexist with each other. This coincidence suggests that the size-induced structural transition is responsible for the dip

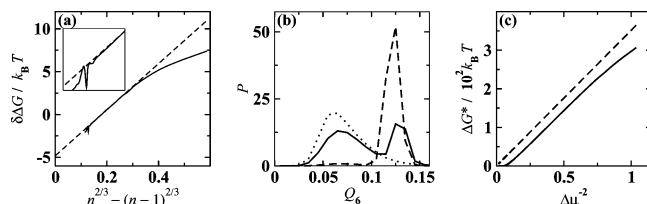


Figure 10. (a) $\delta\Delta G(n)$ curve obtained from the NFE results calculated at $T = 0.35$ and $n_v = 1.6 \times 10^{-5}$ (solid) versus that predicted by the CNT (dashed); (b) normalized probability distribution along the crystalline order parameter Q_6 for clusters containing 130 (dotted), 140 (solid), and 150 (dashed) particles; and (c) comparison of the critical nucleation barrier height between the simulation (solid) and the CNT (dashed) in the aggregation step as function of $(\Delta\mu)^{-2}$. The inset in panel (a) magnifies the dip and the deviation of the simulation results from the straight-line behavior toward large clusters (due to the spontaneous freezing of the liquid clusters).

on the $\delta\Delta G$ curves. In particular, at the transition cluster sizes there are twice as many structures (one ordered and the other disordered) that are accessible for the cluster compared with either smaller or larger clusters, which entropically amounts to a favorable free energy reduction by as much as $k_B T \ln 2$ (maximum reached when both structures are equally probable), comparable to the magnitude of the dip shown on the $\delta\Delta G$ curves. These results also appear to confirm our speculation about the participation of crystal clusters in the aggregation step as part of the reason for the sharp increase in the $p^{\text{CNT}}/p^{\text{EXP}}$ onset ratios below 55 K for the argon vapor.

Comparison with CNT and Previous Theoretical Studies on the Crystal Nucleation Barrier Height and Critical Crystal Cluster Size. As mentioned above, the same set of CNT equations can be applied to the crystal nucleation event given that it occurs in a homogeneous bulk phase (i.e., an infinite vapor or liquid system). Although the crystal nucleation described here happens in a finite liquid-like cluster, the cluster system can be used to mimic the liquid phase when its size is sufficiently large. The $\delta\Delta G$ results shown above are clear evidence of this, and quantitative agreements with bulk-phase simulation results have been obtained from cluster-based systems for solvated solute properties such as relative free energies between different solute conformations.⁵⁶ The crystal nucleation free energy calculations described here can be actually made equivalent to a solvation problem. In particular, at high temperatures, as evident from a visual inspection of the configurations and also from the later crystallite analysis, the outer-layer of the cluster is always liquid-like and the developing crystallite is mostly located in the interior of the cluster and can be viewed as being solvated. Thus, the whole system can be divided into a solute, an inner region just large enough to hold the critical crystallite, and an increasingly larger solvent outer-layer, with the growth of the overall cluster size. When the solvent outer-layer is sufficiently thick, the free energy differences between various solute conformations (i.e., ordered versus disordered) are expected to converge to the bulk-phase limit in a similar vein to the ion-pair system described in ref 56. However, for the crystal nucleation case, considering that both “solute” and “solvent” are made of the same particles, a clear boundary for these two regions is difficult to define and would be artificial as it introduces additional constraints (i.e., on the shape and geometry of the critical crystallite) that may be unrealistic. It may also be unnecessary as the Steinhardt Q_6 order parameter calculated for the whole cluster can be fairly indicative of the crystallinity of the inner “solute”. Even for large bulk-phase systems, this order parameter was frequently used as one of the major reaction coordinates for the crystal

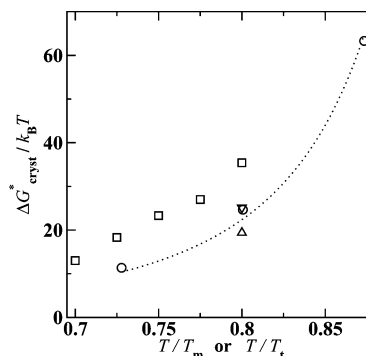


Figure 11. Crystal nucleation barrier height as a function of the degree of undercooling (measured as either T/T_l or T/T_m). The results obtained from this work (based on the NFE profiles shown in Figure 2) or the bulk-phase simulations by Trudu et al. or by ten Wolde et al. were shown as circles, squares, and triangles, respectively. The dotted line represents the CNT prediction.

nucleation process.^{3,29–31} For clusters, the crystallinity of the developing crystallite inside these small systems can be better picked up by the Q_6 parameter. Indeed, as shown in Figure 3, the top of the NFE barrier occurs at a much larger Q_6 value (which is distinctly separated from that of the disordered LFEM) compared with previous bulk-phase nucleation simulations.³ In addition, these profiles obtained at the different cluster sizes appear to yield similar barrier heights (except toward the low temperatures where a precise estimate of the barrier height is probably not so crucial), which resembles the convergence behavior observed in ref 56 for the ion-pair cases solvated by clusters of growing size.

Similar to the vapor–liquid nucleation, the comparison to previous theoretical studies and the CNT for the crystal nucleation step remains focused on the barrier height and the critical cluster size. In particular, in a recent bulk phase study by Trudu et al.,³⁰ the T -dependence of the crystal nucleation barrier height has been carefully examined through molecular dynamics simulations at undercooling conditions from 20% to 30% below the melting point. Plotted in Figure 11 is a comparison between our $\Delta G^*_{\text{cryst}}$ data and theirs as a function of the undercooling condition (described either in terms of T/T_l or T/T_m). Despite the persistent offset between these two sets of data, both show a similar trend with $\Delta G^*_{\text{cryst}}$ diminishing toward deep undercooling conditions, which also agrees with the prediction of spinodal effects from mean field theories.^{30,57–59} This offset is likely caused by the different simulation conditions employed in the two studies. For example, their calculations were performed on a system of 6912 particles with periodic boundary condition at a high pressure of 0.25 kbar (which will result in a higher melting point).³⁰ As shown in the next paragraph, $\Delta G^*_{\text{cryst}}$ is not only sensitive to the degree of undercooling but also explicitly dependent upon the absolute temperature (a major factor affecting the solid–liquid surface tension). The bulk-phase simulations carried out at another set of conditions by ten Wolde et al.³ actually yielded $\Delta G^*_{\text{cryst}}$ values similar to ours.

The comparison to the CNT again requires the input of the bulk-phase properties. Here, we directly computed the number density for the solid phase and the chemical potential difference between the solid and liquid down to the temperature of 0.5 by integrating the following equation,⁶⁰

$$\frac{\Delta\mu}{T} = \int \frac{\Delta\bar{H}}{T^2} dT \quad (10)$$

where $\Delta\bar{H}$ is the molar enthalpy change between the two condensed phases, which can only be determined when the liquid phase is stable over a reasonable simulation length that allows for a precise statistical average. The surface tension calculations are expected to be more troublesome as the solid phase is required to be in direct contact with the liquid phase and the total simulation length is typically on the order of a million Monte Carlo cycles even with a very efficient method⁶¹ (during which the whole system would freeze into a solid lattice). Fortunately the solid–liquid surface tension for the LJ system can be approximated by that of a hard-sphere system whose value can be conveniently evaluated from the formula: $\gamma_0(\text{HS}) = 0.617k_B T/\sigma_{\text{HS}}^2$.⁶² As shown in ref 62, this hard-sphere formula can provide a quantitative description of the interfacial free energy for the simple LJ model with face-centered cubic crystal structures. Following Davidchack and Laird,⁶² the σ_{HS} parameter was replaced by an effective hard-sphere diameter for the LJ system, which was evaluated using the Barker–Henderson criterion⁶³ from liquid-state perturbation theory,

$$\sigma_{\text{eff}} = \int_0^\infty \{1 - \exp[-u_r(r)/k_B T]\} dr \quad (11)$$

where $u_r(r)$ is the reference repulsive part of the potential defined in the Week–Chandler–Anderson theory.⁶³ By substituting these bulk-phase properties in eq 5, the crystal nucleation barrier heights predicted by the CNT were computed, which were also included in Figure 11. Remarkably, despite the approximate nature of the CNT (and also the comparison carried out here), the CNT curve nearly passes through all three simulation points included in this figure. This good agreement with the CNT was also found previously by ten Wolde et al.³ for one of their simulation points at $T = 0.6$. The significant deviation found for the other point at $T = 0.92$ was mostly due to the use of the same surface tension of 0.35 for computing the CNT barrier heights. For example, using the above hard-sphere formula, a surface tension of 0.347 was obtained at $T = 0.6$ versus 0.547 at $T = 0.92$. This increase of about 50% in the surface tension (caused mostly by the increase of the temperature) affects the CNT prediction by a factor of 3, which apparently agrees with the magnitude of the discrepancy reported there.³ The surface tension difference is likely one of the major reasons responsible for the offset observed between Trudu et al.'s data³⁰ and ours (or the CNT predictions). However, toward deep undercooling conditions, the barrier heights provided by the CNT would eventually deviate as it misses the prediction of spinodal effects.

The comparison of the critical crystalline cluster size to the CNT is more problematic as the NFE profiles calculated here from the simulation were not explicitly expressed along this coordinate, and previous bulk-phase simulations³ show that this property is sensitive to its definition. Nevertheless, we took out the configurations located near the top of the barrier (i.e., with a Q_6 value around 0.1) to analyze the size of the biggest crystallite inside the cluster. The definition of this crystallite follows ref 3. Specifically, for every particle i , a normalized 13-dimensional complex vector $q_6(i)$ was defined with its m th component given by,

$$q_{6m}(i) = \frac{\bar{q}_{6m}(i)}{\left[\sum_{m=-6}^6 |\bar{q}_{6m}(i)|^2 \right]^{1/2}} \quad (12)$$

where q_{6m} is a local bond-order parameter which can be obtained in a similar way to Q_{6m} (see eq 2) by summing over only the

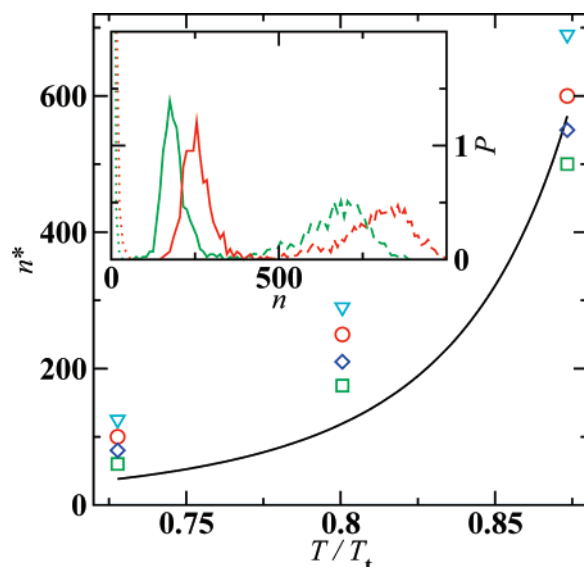


Figure 12. Critical crystal cluster size predicted by the CNT (solid line) versus the average size of the largest crystallite contained by clusters with an overall Q_6 value between 0.09 and 0.11 as a function of the degree of undercooling. Triangles, circles, diamonds, and squares represent the simulation results using an n_t value of 7, 8, 9, and 10, respectively. Shown in the inset are the size distributions of these crystallites obtained at $T = 0.55$ using an n_t of 8 (red) or 10 (green). Also included are the size distributions of the crystallite contained by clusters with an overall Q_6 value less than 0.05 (dotted line) or larger than 0.18 (dashed line). Only clusters with a minimum size of 700 at $T = 0.5$, of 1400 at $T = 0.55$, or of 3200 at $T = 0.6$ are selected for this analysis.

bonded pairs connected to particle i . For the solid system, it is the coherence of this local order parameter that adds up to a nonzero Q_6 . To determine whether two neighboring particles (say, i and j) are in phase with one another, we calculated the dot product of the vector \mathbf{q}_6 . Only when this dot product $q_6(i) \cdot q_6(j)$ exceeds 0.5 are these two particles considered connected to each other. Furthermore, a particle is classified as solid-like only when it has at least a certain number of in-phase connections (varied between 7 and 10). Finally, we applied the typical Stillinger cluster criterion to the solid particles to find the largest crystallite inside the whole system.

Plotted in Figure 12 is a comparison between the average size of the largest solid cluster contained by those configurations with a sufficiently large cluster size and a Q_6 value between 0.09 and 0.11 and the critical crystalline cluster size predicted by the CNT. Note that the simulation data are fairly sensitive to the solid-cluster criteria. For example, a change in the threshold number of the in-phase connections (n_t) from 7 to 10 (for determining whether a particle is solid-like or not) leads to a significant shift of the solid cluster sizes to lower numbers for all conditions. However, even with the most stringent threshold of 10, toward the deep undercooling conditions, the simulation data were still above the n^* value predicted by the CNT. Only at the low undercooling conditions did the simulation appear to yield similar sizes to the CNT. For example, at $T = 0.6$ (corresponding to a 13% undercooling condition), a nearly perfect agreement can be obtained between the simulation and the CNT when n_t is somewhere between 8 and 9. Although the average sizes obtained from the simulation show a clear separation from the CNT results, the size distributions of the largest crystallite obtained from those critical configurations are rather broad. Plotted in the inset of Figure 12 are two representative sets of distributions obtained at $T = 0.55$ with either 8 or 10 for n_t . These distributions are constructed

(separately) not only for the critical configurations but also for two other important groups of configurations, one representing the LFEM (with Q_6 below 0.05) and the other the CFEM (with Q_6 above 0.18). For all of them except the LFEM case, the size of the largest crystallite contained by each individual group of configurations spans a wide range. In fact, with these distributions being so broad, the sizes of the smallest crystallite contained by those critical configurations are approaching or already overlapped with the n^* value predicted by the CNT at even the low T conditions. Despite this broadness, the distributions obtained for each individual group of configurations are distinctly separated from each other, irrespective of the solid-cluster criterion. Thus, the correlation between the Q_6 and the size of the largest crystallite (a local indicator of the crystallinity) is prominent, which provides another justification for the use of this order parameter. However, at the low temperatures (already at $T = 0.5$), a bimodal distribution (not shown here) was sometimes observed for the critical configurations determined solely based on the Q_6 value with one centered on a surprisingly large size, indicating that clusters containing a very big (but low quality) crystallite can still have a relatively small Q_6 value. This is consistent with the lack of a distinct peak position on the NFE profiles toward lower temperatures (see Figure 3), and the fact that the crystal nucleation free energy barrier is so low that ramification of multiple small crystallites can sometimes occur, which was also found previously in bulk-phase simulations.³⁰ For those cases, the distribution centered around the smaller value was used to determine the average size of the crystallite included in Figure 12.

D. Microscopic Structures of the Clusters. One of the major assumptions made by the CNT is that clusters are compact and spherical. This is contradicted by the fractal nature of the initial droplets formed in the vapor–liquid nucleation process, which has been already shown from our previous simulations for the LJ system at temperatures above T_l . The dimensionality of the clusters can be measured from the slope of the log–log plot of the aggregation number versus the r_g (radius of gyration) parameter (see Figure 13a). For compact and spherical aggregates, a slope of three is expected, while for small clusters, a much smaller slope was actually observed. Only when clusters are large enough do they start to behave like a three-dimensional object. Thus, the whole curve displayed a pronounced “S” shape, with the dimensionality transition occurring at larger cluster sizes at higher temperatures, which is consistent with our previous findings.¹¹

Compared with the vapor–liquid nucleation, the initial crystallites formed in the crystal nucleation process are more compact. For example, at $T = 0.6$ for the same aggregation number of 10, the crystallite has a smaller r_g than the liquid droplet by about 12%. On the contrary, for higher aggregation numbers, the crystallite shows larger r_g values than the same-size liquid droplets. Correspondingly, the “S” shape character (denoting the dimensionality transition) is less obvious on the log–log plots shown in Figure 13b. Visual inspection of the snapshots (see Figure 14) indicates that the particles located at the outer-layer of the solid cluster (determined using the criterion described above) are very loosely attached even for large crystallites, presumably because of their tendency to be dissolved by the surrounding liquid. The interface between the crystallite and the liquid is rather diffuse, which is also evident from Figure 15, where both density and the average number of in-phase connections per particle (n_c) were plotted as function of the radial distance from the center of the largest crystallite. Toward the center of the crystallite, both ρ and n_c approach the bulk-

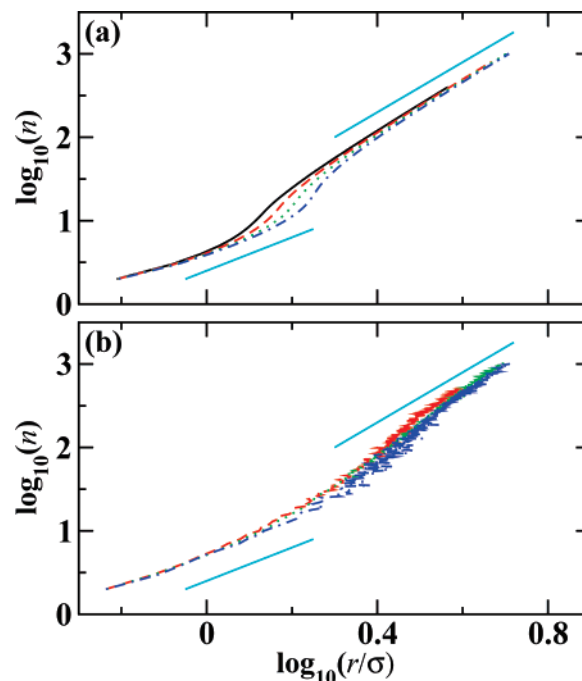


Figure 13. Log–log plot of the size of (a) the liquid droplet or (b) the crystallite versus the radius of gyration obtained at $T = 0.45$ (solid), 0.5 (red dashed), 0.55 (green dotted), and 0.6 (blue dashed-dotted). The two straight lines are drawn as a guide to the eye with slopes of 2 (lower) and 3 (upper).

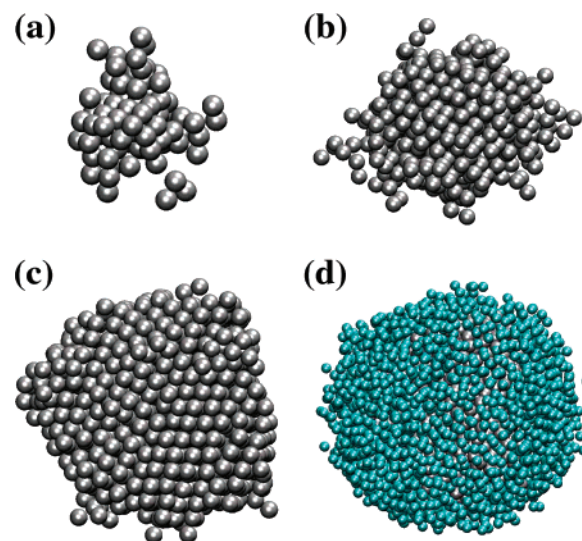


Figure 14. Snapshots of the crystallites containing (a) 86, (b) 559, and (c) 1286 particles. For the last crystallite, the whole cluster configuration was shown in (d), which includes the surrounding liquid particles, colored in cyan.

solid values (in particular for sufficiently large crystallites), while at the crystallite–liquid interface, these properties show a decay toward the bulk-liquid value. Based on these profiles, a rather wide crystallite–liquid interface can be resolved with the critical radius predicted by the CNT located within this window. However, in the CNT only a sharp interface is assumed and both ρ and n_c would reach the bulk-liquid value at the same position. This assumption apparently breaks down again for the crystallite–liquid interface. In addition, Figure 15 indicated that the density profile reaches the bulk-liquid value first, which suggests that around the crystallite there is an ordered “shell” with liquid-like density. This result has been found in previous bulk-phase simulation by ten Wolde et al.³ and the DFT

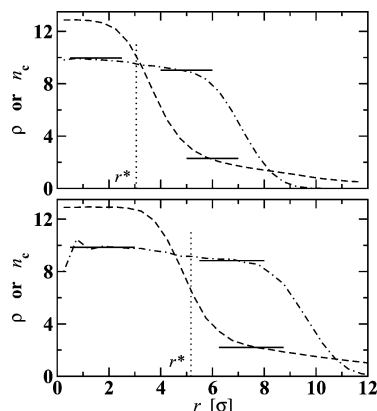


Figure 15. Density (dashed-dotted) and the average number of in-phase connections per particle (dashed) as a function of the radial distance from the center of the largest crystallite analyzed for clusters with an overall Q_6 value between 0.09 and 0.11 and a minimum size as in Figure 12. The densities are scaled up by a factor of 10. r^* is the radius of the critical nucleus predicted by the CNT using eq 6. The horizontal lines were drawn as a guide to denote the bulk-phase values. The top and bottom panels represent the results obtained at $T = 0.55$ and 0.6, respectively.

calculation by Harrowell and Oxtoby.⁶⁴ Other than the diffuse interface, the crystallites look fairly compact and are very well-solvated by the surrounding liquid layers (see Figure 14).

From the above structural analysis, the approximate nature of the CNT is evident. Furthermore, for the vapor–liquid nucleation, direct connections can be made between the structural deviations and the discrepancies observed in the nucleation results. In particular, when comparing Figure 13 to Figures 4–6, it is immediately clear that the $\delta\Delta G$ differences are mainly present for those fractal, low-density aggregates and soon after the clusters take a three-dimensional shape, both $\delta\Delta G$ and n^* predicted by the CNT are right on the curve yielded from the simulation. This nearly perfect performance comes too late for the theory, and the $\delta\Delta G$ deviations found for the initial clusters already accumulate into a large offset (the so-called $B(T)$ term).^{14,65,66} This offset, combined with the other erroneous $A_{1\gamma}$ term, affects the ΔG value for the entire spectrum of clusters formed thereafter (including ΔG^*). On the other hand, considering that the crystallites formed at the beginning of the crystal nucleation are relatively more compact and that a much smaller $A_{1\gamma}$ term would come out of the significantly reduced solid–liquid interfacial tension, the improved predictions by the CNT on the crystal nucleation barrier heights are actually expected for this simple LJ system. However, it would be interesting to find out whether this theory would maintain such a good performance for crystal nucleation processes encountered by more complicated molecular systems, and the simulation method described here can be extended to those models.

4. Conclusions

The AVUS-HR technique that has led to our recent success in vapor–liquid nucleation research was extended to the study of the nucleation processes encountered by a super-saturated Lennard-Jones vapor at temperatures below the triple point. In particular, by introducing the Steinhardt order parameter Q_6 as an additional reaction coordinate for the description of the nucleation landscape, this method allows a detailed examination of crystal nucleation events in cluster systems. It was found that the crystal formation process in these LJ clusters proceeds via two separate nucleation steps, first a vapor–liquid like aggregation followed by the nucleation of crystals inside the

aggregates, except at very low temperatures where the crystal nucleation barrier was found to be negligible. The disappearance of the crystal nucleation barrier toward deep undercooling conditions is consistent with a recent molecular dynamics study for the bulk LJ systems and also with the prediction of spinodal effects from mean field theories, which are missing in the classical theory. Other than the absence of the spinodal effects, at low undercooling conditions, the CNT predicts crystal nucleation barrier heights that are reasonably close to the simulation data. On the contrary, for the vapor–liquid nucleation step, much larger deviations were observed in the nucleation barrier heights. In agreement with previous simulation analysis on this type of nucleation, these deviations mainly arise from the discrepancies observed for the smallest clusters, including a nonzero $A_{1\gamma}$ term used by the theory in describing the monomer work of formation. Toward deep undercooling conditions, the barrierless crystallization leads to additional errors for the CNT as the crystalline clusters can be no longer described using liquid-like properties. The structural analysis further provided a microscopic origin of this failure. In particular, the initial aggregates formed are fractal and loosely packed, and thus cannot be modeled as compact droplets with liquid-like densities. This comprehensive analysis of the vapor–liquid nucleation also left a hint on why better results were predicted by the CNT for the crystal nucleation process. This is due to the more compact crystallites formed at the beginning of this event and the significantly reduced $A_{1\gamma}$ term. Given the simplicities of the theory, its nearly perfect description of the LJ system (especially for the crystal nucleation and most clusters formed in the vapor–liquid nucleation) is remarkable. However, it remains uncertain to what limit we can apply this theory to the study of the crystal nucleation events. Thus, further work is planned, in a similar way to the progress made recently in the vapor–liquid nucleation, to extend the application of the simulation method described here to more complex molecular systems.

Acknowledgment. Financial support from the LSU start-up fund, the National Science Foundation (CHE/MCB-0448918), the Petroleum Research Fund, administered by the American Chemical Society (Grant 41933-G9), Louisiana Board of Regents Support Fund (LEQSF(2005-08)-RD-A-02), and a Council on Research Summer Stipend Award from LSU Office of Research and Graduate Studies is gratefully acknowledged. Part of the computer resources were provided by the Center for Computation and Technology, the Office of Computing Services at LSU, and the Louisiana Optical Network Initiative.

References and Notes

- (1) Dunitz, J. D.; Bernstein, J. *Acc. Chem. Res.* **1995**, *28*, 193.
- (2) Brittain, H. G. *Polymorphism in Pharmaceutical Solids*; Marcel Dekker, Inc.: New York, 1999.
- (3) ten Wolde, P. R.; Ruiz-Montero, M. J.; Frenkel, D. *J. Chem. Phys.* **1996**, *104*, 9932.
- (4) Becker, R.; Döring, W. *Ann. Phys.* **1935**, *24*, 719.
- (5) Volmer, M. *Kinetik der Phasenbildung*; Steinkopff: Dresden, 1939.
- (6) Reiss, H. *J. Chem. Phys.* **1950**, *18*, 840.
- (7) Laaksonen, A.; Talanquer, V.; Oxtoby, D. W. *Annu. Rev. Phys. Chem.* **1995**, *46*, 489.
- (8) Stauffer, D. *Aerosol. Sci.* **1976**, *7*, 319.
- (9) Wilemski, G. *J. Phys. Chem.* **1987**, *91*, 2492.
- (10) Jaeger-Voirol, A.; Mirabel, P.; Reiss, H. *J. Chem. Phys.* **1987**, *87*, 4849.
- (11) Chen, B.; Siepmann, J. I.; Oh, K. J.; Klein, M. L. *J. Chem. Phys.* **2001**, *115*, 10903.
- (12) Chen, B.; Siepmann, J. I.; Oh, K. J.; Klein, M. L. *J. Chem. Phys.* **2002**, *116*, 4317.
- (13) Chen, B.; Siepmann, J. I.; Klein, M. L. *J. Am. Chem. Soc.* **2003**, *125*, 3113.

- (14) Merikanto, J.; Zapadinsky, E.; Lauri, A.; Vehkamäki, H. *Phys. Rev. Lett.* **2007**, *98*, 145702.
- (15) Nellas, R. B.; Chen, B.; Siepmann, J. I. *Phys. Chem. Chem. Phys.* **2007**, *9*, 2779.
- (16) Chen, B.; Siepmann, J. I.; Klein, M. L. *J. Phys. Chem. A* **2005**, *109*, 1137.
- (17) Nellas, R. B.; McKenzie, M. E.; Chen, B. *J. Phys. Chem. B* **2006**, *110*, 18619.
- (18) Chen, B.; Siepmann, J. I. *J. Phys. Chem. B* **2000**, *104*, 8725.
- (19) Chen, B.; Siepmann, J. I. *J. Phys. Chem. B* **2001**, *105*, 11275.
- (20) Siepmann, J. I.; Frenkel, D. *Mol. Phys.* **1992**, *75*, 59.
- (21) Frenkel, D.; Mooij, G. C. A. M.; Smit, B. *J. Phys.: Condens. Matter* **1992**, *4*, 3053.
- (22) Martin, M. G.; Siepmann, J. I. *J. Phys. Chem. B* **1999**, *103*, 4508.
- (23) Torrie, G. M.; Valleau, J. P. *Chem. Phys. Lett.* **1974**, *28*, 578.
- (24) Wilding, N. B. *Phys. Rev. E* **1995**, *52*, 602.
- (25) Potoff, J. J.; Panagiotopoulos, A. Z. *J. Chem. Phys.* **1998**, *109*, 10914.
- (26) Metropolis, N.; Rosenbluth, A. W.; Rosenbluth, M. N.; Teller, A. H.; Teller, E. *J. Chem. Phys.* **1953**, *21*, 1087.
- (27) Stillinger, F. H. *J. Chem. Phys.* **1963**, *38*, 1486.
- (28) Steinhardt, P. J.; Nelson, D. R.; Ronchetti, M. *Phys. Rev. B* **1983**, *28*, 784.
- (29) van Duijneldt, J. S.; Frenkel, D. *J. Chem. Phys.* **1992**, *96*, 4655.
- (30) Trudu, F.; Donadio, D.; Parrinello, M. *Phys. Rev. Lett.* **2006**, *97*, 105701.
- (31) Moroni, D.; ten Wolde, P. R.; Bolhuis, P. G. *Phys. Rev. Lett.* **2005**, *94*, 235703.
- (32) ten Wolde, P. R.; Frenkel, D. *J. Chem. Phys.* **1998**, *109*, 9901.
- (33) Kusaka, I.; Wang, Z.-G.; Seinfeld, J. H. *J. Chem. Phys.* **1998**, *108*, 3416.
- (34) Martin, M. G.; Siepmann, J. I. *J. Phys. Chem. B* **1999**, *103*, 4508.
- (35) Esselink, K.; Loyens, L. D. J. C.; Smit, B. *Phys. Rev. E* **1995**, *51*, 1560.
- (36) Chen, B.; Siepmann, J. I.; Klein, M. L. *J. Phys. Chem. B* **2001**, *105*, 9840.
- (37) Mendez-Villuendas, E.; Saika-Voivod, I.; Bowles, R. K. *J. Chem. Phys.* **2007**, *127*, 154703.
- (38) Rowlinson, J. S.; Widom, B. *Molecular Theory of Capillarity*; Clarendon: Oxford, 1982.
- (39) Salomons, E.; Mareschal, M. *J. Phys.: Condens. Matter* **1991**, *3*, 3645.
- (40) Harris, J. G. *J. Phys. Chem.* **1992**, *96*, 5077.
- (41) Mecke, M.; Winkelmann, J.; Fischer, J. *J. Chem. Phys.* **1997**, *107*, 9264.
- (42) Panagiotopoulos, A. Z. *Mol. Phys.* **1987**, *61*, 813.
- (43) Panagiotopoulos, A. Z.; Quirke, N.; Stapleton, M.; Tildesley, D. J. *Mol. Phys.* **1988**, *63*, 527.
- (44) Smit, B.; de Smedt, P.; Frenkel, D. *Mol. Phys.* **1989**, *68*, 931.
- (45) Hale, B. N. *Aust. J. Phys.* **1996**, *49*, 425.
- (46) McGraw, R.; Laaksonen, A. *J. Chem. Phys.* **1997**, *106*, 5284.
- (47) Fladerer, A.; Strey, R. *J. Chem. Phys.* **2006**, *124*, 164710.
- (48) Martin, M. G.; Siepmann, J. I. *Theor. Chem. Acc.* **1998**, *99*, 347.
- (49) Sprow, F. B.; Prausnitz, J. M. *Trans. Faraday Soc.* **1966**, *62*, 1097.
- (50) Stewart, R. B.; Jacobsen, T. *J. Phys. Chem. Ref. Data* **1989**, *18*, 639.
- (51) Wagner, W. *Cryogenics* **1973**, *13*, 470.
- (52) Haynes, W. M. *Cryogenics* **1978**, *18*, 621.
- (53) Seok, C.; Oxtoby, D. W. *J. Chem. Phys.* **1998**, *109*, 7982.
- (54) Courtney, W. G. *J. Chem. Phys.* **1961**, *35*, 2249.
- (55) <http://webbook.nist.gov>.
- (56) Keasler, S. J.; Nellas, R. B.; Chen, B. *J. Chem. Phys.* **2006**, *125*, 144520.
- (57) Klein, W.; Leyvraz, F. *Phys. Rev. Lett.* **1986**, *57*, 2845.
- (58) Cahn, J. W.; Hilliard, J. E. *J. Chem. Phys.* **1959**, *31*, 688.
- (59) Unger, C.; Klein, W. *Phys. Rev. B* **1984**, *29*, 2698.
- (60) McQuarrie, D. A.; Simon, J. D. *Physical Chemistry, A Molecular Approach*; University Science Books: Sausalito, 1997.
- (61) Mu, Y.; Song, X. *J. Chem. Phys.* **2006**, *124*, 034712.
- (62) Davidchack, R. L.; Laird, B. B. *J. Chem. Phys.* **2003**, *118*, 7651.
- (63) Hansen, J. P.; McDonald, I. R. *Theory of Simple Liquids*, 2nd ed.; Academic: New York, 1986.
- (64) Harrowell, P.; Oxtoby, D. W. *J. Chem. Phys.* **1984**, *80*, 1639.
- (65) Hale, B. N. *Metall. Trans. A* **1992**, *23*, 1863.
- (66) Hale, B. N.; DiMattio, D. J. *J. Phys. Chem. B* **2004**, *108*, 19780.